

Spring 5-13-2017

Simulation and Analysis of the Band-Agile Coaxial Backward-Wave Oscillator

Phillip H. Fansler
University of New Mexico

Follow this and additional works at: https://digitalrepository.unm.edu/ece_etds



Part of the [Electrical and Computer Engineering Commons](#)

Recommended Citation

Fansler, Phillip H.. "Simulation and Analysis of the Band-Agile Coaxial Backward-Wave Oscillator." (2017).
https://digitalrepository.unm.edu/ece_etds/362

This Thesis is brought to you for free and open access by the Engineering ETDs at UNM Digital Repository. It has been accepted for inclusion in Electrical and Computer Engineering ETDs by an authorized administrator of UNM Digital Repository. For more information, please contact disc@unm.edu.

Phillip Fansler

Candidate

Electrical and Computer Engineering

Department

This thesis is approved, and it is acceptable in quality and form for publication:

Approved by the Thesis Committee:

Dr. Jane Lehr

, Chairperson

Dr. Edl Schamiloglu

Dr. Peter Mardahl

Simulation and Analysis of the Band-Agile Coaxial Backward-Wave Oscillator

by

Phillip Fansler

B.S., Mining and Minerals Engineering, Virginia Tech, 2012

THESIS

Submitted in Partial Fulfillment of the
Requirements for the Degree of

Master of Science in Electrical Engineering

The University of New Mexico

Albuquerque, New Mexico

July, 2017

Simulation and Analysis of the Band-Agile Coaxial Backward-Wave Oscillator

by

Phillip Fansler

B.S., Mining and Minerals Engineering, Virginia Tech, 2012

M.S., Electrical Engineering, University of New Mexico, 2017

Abstract

Simulation of a Band-Agile Coaxial Backward-Wave Oscillator (BACoRBWO) produced a device that is tunable to operate in two distinct bands: L-band ($1.4GHz$) at $1.9GW$ with an efficiency of 26%, and C-band ($4.2GHz$) at $1.1GW$ with an efficiency of 15%. The device does not perform as expected based on existing literature; however the end result is not necessarily undesirable. The need for further exploration of the discrepancies between contemporary literature and our findings notwithstanding, this device operates well enough of its own accord to merit additional study.

Contents

List of Figures	v
List of Tables	vii
Introduction	1
Methods	7
Automation of Data Processing and Visualization	12
Results	20
Discussion	25
Conclusions	31
References	33

List of Figures

Figure 1: Geometry of the BACoRBWO in Coaxial Configuration	5
Figure 2: Geometry of the BACoRBWO in Hollow Configuration	5
Figure 3: Data Processing Flowchart	11
Figure 4: Power Spectrum of the Coaxial-Mode BACoRBWO	23
Figure 5: Power Spectrum of the Hollow-Mode BACoRBWO	23
Figure 6: Power and Frequency vs. Inner Conductor Length	23
Figure 7: Electron Velocity vs. Axial Position (<i>Voltage</i> = 760kV)	23
Figure 8: Efficiency and Voltage vs. Frequency (Coaxial Configuration)	24
Figure 9: Efficiency and Voltage vs. Frequency (Hollow Configuration)	24
Figure 10: Power Output vs. Time (Coaxial)	24
Figure 11: Power Output vs. Time (Hollow)	24
Figure 12: Particle Kinetic Energy vs. Axial Distance	27
Figure 13: Electron Velocity vs. Axial Distance (<i>Voltage</i> = 660kV)	27
Figure 14: Dispersion Diagram (Coaxial Configuration)	28

LIST OF FIGURES

vi

Figure 15: Dispersion Diagram (Hollow Configuration) 28

List of Tables

Table 1: MakeGRB.py Function Summary	19
--	----

Introduction

The Backward-Wave Oscillator (BWO) is a High-Power Microwave (HPM) source; these devices primarily find their use (in the Air Force) in Directed Energy (DE) weaponry as the component that creates the high-powered Radio Frequency (RF) waves that disrupt the operation of hostile targets. Low-power (i.e. Watt and kilo-Watt class) BWOs have been in existence for more than 60 years; they were first developed for applications that require a very wide tuning range (such as radar jammers) and marketed under the trade name "Carcinotron". These typically had an output power of no more than 1W [1]. The BWOs being actively researched by the Air Force Research Lab (AFRL) are gigawatt-class HPM sources. Needless to say, to scale the output power of the technology by 9 orders of magnitude requires a much larger device, and because this device is so large, it becomes what is known as an overmoded HPM source. An overmoded HPM source has several electromagnetic wave modes that can propagate in addition to the desired output; these modes can interfere with the output and attenuate the power. This is not an insurmountable problem, however it takes thorough design and simulation work to ensure that only the proper mode is allowed to resonate and emit from the device.

The US Air Force is interested in the weaponization of this technology; hence there is a need for a wide array of HPM devices that meet varying criteria such as power output, frequency output, size, etc that will be effective in different warfare

scenarios. Because these devices are so complex and interdependent on other components, improving the size, performance, or efficiency of any one part can then allow other parts to be reduced in size, power requirements, etc. This is a top priority for Air Force DE researchers; less size and weight means that the DE weaponry can be mounted on smaller and more maneuverable platforms such as planes, ground vehicles, or even missiles and drones. When these devices are more maneuverable, they are more effective. One device class that is currently of specific interest to the AFRL is that of a tunable, low-frequency (L-band [$1 - 2GHz$]), high-power ($> 1GW$) device.

There are several constituent components of an HPM source; first in the chain is the pulsed power source, this generates a voltage pulse somewhere between $100kV$ and $1MV$ for $30 - 120ns$. The pulse generating equipment is often housed in a transformer oil bath, and because the HPM source must operate in a vacuum, this necessitates the use of a dividing insulator between the oil and vacuum. This pulse is then fed to an electron gun, which becomes highly negative and emits high velocity electrons into the source cavity. Next, the electrons pass through a periodic Slow-Wave Structure (SWS); this structure acts to decrease the phase velocity of light inside the BWO [2]. When the electrons encounter this structure, they are travelling faster than the local phase velocity of light, causing emission of Čerenkov radiation in their wake (analogous to a sonic boom when an object is travelling faster than the speed of sound). Čerenkov radiation is an electromagnetic (EM) wave, and it is these waves that excite the HPM source's cavity into resonance. The last structure that is part of the BWO is the mode converter and output waveguide; this converts the BWO's resonant mode into waveguide modes that can be radiated. The entire BWO is contained within a magnetic coil that generates a uniform axial magnetic field on the order of 1 Tesla, the purpose of which is two-fold. The magnetic field constrains the electron beam to move axially through the device, rather than letting the beam wander radially and impact the walls; it also suppresses cyclotron resonances which

would absorb the generated RF power. Important to note here is the application of the adjective “Backward-Wave” to this device. The electromagnetic wave we desire to extract from the BWO travels antiparallel to the electron beam i.e. towards the cathode. Schemes exist to extract the RF power near the cathode, but these are hampered by the high static magnetic fields and associated machinery (coils, etc). The problem is overcome by the use of either a cut-off neck or a tuned reflection cavity that allows the electron beam to pass uninhibited but reflects the EM waves of the desired frequency back towards the output waveguide.

From the BWO’s continuous wave, low-power beginnings in the 1950s, it was largely scientifically neglected until 1970 when John Nation at Cornell University published his $10MW$ pulsed version of the tube [3]. His experimental setup utilized a $500kV$, $40kA$ beam in a $1.2T$ field. The efficiency of this device was 0.05%, something he acknowledged “probably indicates that much higher power levels are available with better design.” Four years later, Carmel, in the same lab at Cornell, demonstrated a $500MW$ BWO operating at 17% efficiency [4]. Much of this improvement came from elimination of the microwave breakdown in the SWS that Nation experienced. After these publications, BWO development in the United States languished once again. However, Soviet scientists saw potential in the device and starting in 1973 began a continuous stream of research that lasted through the 1990s. The first results by Kovalev in 1973 at the Lebedev Institute of Physics in Moscow published a 12-15% efficient relativistic BWO (RBWO) [5]. In 1981 $1GW$ of output power (operating at 30% efficiency) was surpassed [6] by Ivanov et al. In 1997, the research team at the Institute of High Current Electronics (IHCE), Russian Academy of Sciences, in Tomsk, Russia tested an RBWO whose output power was greater than $3GW$ [7] and in 2000, they improved the pulse shortening of high energy HPM sources, granting a four-fold increase in energy-per-pulse [8].

Frequency tuning of the BWO can be accomplished by either adjusting the beam energy or by mechanically tuning the dimensions of the device. The original Carcinotron was tunable over a frequency range of approximately an octave by adjusting the beam voltage [1]; RBWOs are tunable in the same manner, but with less bandwidth [4]. However, voltage tuning does not translate well to an RBWO because of the relativistic nature of the device [9]. This therefore leaves mechanical tunability as the preferred method by which to tune the RBWO. One of the techniques used to mechanically tune RBWOs is to vary the beam drift length past a cut-off neck. After the electron gun, but before the slow wave structure, the beam passes this structure, which pre-bunches the electrons before entry into the SWS. The phase of this modulation (dependent on the drift distance between the reflector and SWS) relative to the phase of the harmonic wave in the SWS affects the output frequency. In 1996, Moreland and colleagues tested and simulated a BWO with 4% tuning range using such a cut-off neck [10]. A similar technique was investigated in 2005 by Kitsanov et al (again at the IHCE) using a resonant reflector instead of a cut-off neck and finding a 14% frequency tuning range [9].

The coaxial RBWO (CoRBWO) is an additional refinement of the RBWO. A center conductor is added in the SWS which increases the space-charge limiting current and thus the potential for higher power. Most RBWOs to date have used hollow SWSs, but a few exceptions have been coaxial, including the earliest RBWO referenced (Nation's 1970 design) [3, 11]. Work on the CoRBWO began in earnest with 2006-7 work by (then PhD candidate) Dr. Renzhen Xiao at Tsinghua University; her work numerically solved many relationships for the CoRBWO, including "space-charge limiting current, dispersion relations, dispersion curves, and coupling impedance" [12]. She found efficiencies of 34 and 37% for these devices using numerical and simulation methods, respectively. [13].

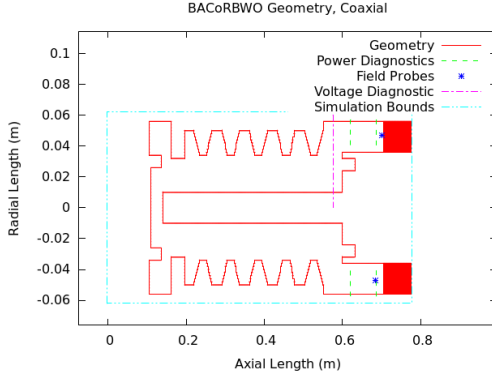


Figure 1: Geometry of the BACoRBWO in Coaxial Configuration.

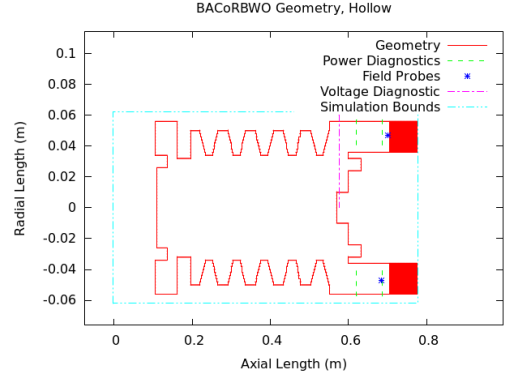


Figure 2: Geometry of the BACoRBWO in Hollow Configuration.

Starting in 2009, a group of researchers led by Dr. Xingjun Ge at China's National University of Defense Technology (NUDT) also started developing gigawatt-class coaxial BWOs [14]; their work was heavily reliant on the earlier work by Xiao. Ge's idea was to use a CoRBWO, but instead of altering the beam drift distance in order to tune, they would mechanically shift the inner conductor towards or further away from the cathode. In addition to frequency tuning the device, retracting the coaxial conductor far enough will have another effect - it will cause the device to change from a coaxial BWO to a hollow BWO, thus shifting the operation band. The first revision of Ge's design for this Band-Agile CoRBWO (BACoRBWO) was published in 2010 [15]. In that paper, they investigated the effect of changing the inner conductor's radius on the output frequency; the researchers found a tunability range of about 4%. In 2014, they published the results of experiments and simulations of a BACoRBWO that was tunable by sliding the inner conductor into or out of the SWS [16]. The geometry of these configurations are re-created in Figures 1 and 2. The axis of radial symmetry is the x -axis, or, where Radial Length = 0. In order to transition between the two configurations, the inner conductor is either extended or retracted from the extractor at the right side of the images. The team found an operating range of $1.61\text{GHz} \pm 8.5\%$ (Coaxial) and $2.32\text{GHz} \pm 2\%$ (Hollow) at 2.0GW and 1.3GW with efficiencies of 31.7% and 20.6%, respectively.

The results found by Ge are most interesting because the ability to radiate multiple bands of RF power from a single device increases its usefulness over a single-band device. Every potential target of an Air Force DE weapon has a preferred frequency at which the weapon will be most effective. The advantage to a band-agile and tunable HPM source then becomes apparent; if a wider range of targets can be disabled or destroyed by a single device, then that means less cost as well as more operational flexibility. The objective of this thesis is to propose to the AFRL a design of a Band-Agile Coaxial Backwards Wave Oscillator capable of operating in multiple bands at powers greater than $1GW$. In order to do this, I intend to replicate the findings in Ge et al's 2014 work, failing that, I will explore the behavior and operation of this device in order to create a working model suitable for the application.

Methods

The software used to create the simulations was the Improved Concurrent Electromagnetic Particle In Cell (ICEPIC) program. ICEPIC has been validated using real-world data and has been used in many publications affiliated with the AFRL [17, 18]. In essence, a Particle-in-Cell code computes the particle positions and velocities as well as the field strengths at every time step, for every cell in the simulations. Depending on the granularity needed for the simulation, these computations can be quite onerous. However, the AFRL has at its disposal the Department of Defense's High Performance Computing (HPC) machines; these allow myriad simulations to be run in a reasonable amount of time.

The first logical step in creating a band-agile HPM source was to reproduce the work by Ge that has already been published. Dimensions of Ge's device were published in his 2014 paper[16]; these specifications were used to create a simulation file for ICEPIC. Two different configurations of the BWO were tested, coaxial (with the center conductor in place or extended) and hollow (with the center conductor absent or retracted). In each configuration the beam parameters were forced to the desired values to ensure consistency. In practice, an electron gun would need to be designed to emit the desired beam and a voltage pulse would be applied to the electron gun to emit the beam; however, this design problem is out of the scope of this project. The initial beam parameters reflected the values used in Ge's publication, specifically, the

diode voltage was set to $760kV$, the beam current to $9.6kA$, and the confining magnetic field to $1.1T$. With these parameters, the coaxial configuration should oscillate at $1.61GHz$ and the hollow configuration should oscillate at $2.32GHz$.

The simulations ramped the beam voltage up linearly to the maximum over a $10ns$ period. After this, the beam was sustained for another $90ns$; this allowed plenty of time to see the start-up characteristics of the device as well as observe how the device behaved once competing modes were given time to build up and potentially cause interference with the signal. Many types of data were collected from the simulations. These included currents through each part of the device and SWS, power through the output waveguide broken down by propagation mode, E and B-Field values for every cell in the simulation and particle positions and velocities for every particle emitted.

ICEPIC, after being sent the dimensions of the object to be simulated, converts the structure into an array of rectangular prisms; in this case, the grid had a $2mm$ resolution in all 3 dimensions. This gridded structure is detailed in Figures 1 and 2 on page 5. The time step is determined at runtime by ICEPIC, and the simulations created for this paper used time steps of approximately 3-4 picoseconds. Power output was measured from the Poynting flux through the plane of interest (the output waveguide).

Because the objective of this simulation is the virtual prototype of a band-agile and tunable HPM source, the nature of the tunability was investigated by varying the length of the inner conductor (as per the NUDT's work, see [14, 19, 20, 21, 15, 22, 16]). The particular length of inner conductor that caused the device to jump from one band to the other is of interest, as well as the relationship between length and intra-band tunability. Additionally, because BWOs have traditionally been tunable by voltage changes [1], the response of the BWO was measured as the voltage was varied over a wide range, despite assertions made in Kitsanov's work [9]. This gave an idea of how

sensitive the device operation is to voltage changes as well as allowed us to explore theories about how operation of the BWO may be improved or expanded upon.

The electron beam was functionally characterized in two ways, the first of which was a spatial analysis of the beam’s energy content. At each position of axial length along the beam path, the kinetic energy of every constituent particle of the beam was measured and averaged across time points to give a profile of the beam’s per-particle energy content. From this information, an estimation of the maximum possible RF emission efficiency for that configuration was computed from the percentage difference between the leftmost (i.e. closest to the electron gun) particle energy and the rightmost (closest to the extractor) particle energy. This calculation will give a upper limit on output efficiency for that specific configuration; not all of this energy given up by the particles will be emitted from the BWO as useful radiation.

The other tool used to characterize the electron beam was the dispersion diagram (for an example, see Figures 14 and 15 on page 28). On the y-axis is shown frequency, in either cycles or radians per unit time, and on the x-axis is shown wavenumber, in either cycles or radians per unit distance. Wavenumber is defined as the inverse wavelength. The phase velocity is ω/k , and the group velocity is $d\omega/dk$, where ω is the angular frequency and k is the wavenumber. In order for a backward wave to form, the group velocity must be negative at the beam interaction point. Also shown on the dispersion diagram is the “light line”, the plot of an EM waves’ frequency as a function of wavenumber, where $f/k = c$, f is the frequency and c is the speed of light in vacuum, and the “beam line”, the plot of the electron beam’s velocity as a function of f and k (anywhere from $0.3 - 0.9c$). The dispersion relationship was found through “cold-cavity” simulations, meaning that there is no electron beam present during the measurement. In order to increase the spatial resolution to a usable level, the slow wave structure present in the BACoRBWO was extended to 54 periods (in contrast

to the 5 used for the actual device). The cavity was excited by a 1 Amp signal from 4 antennas at the upstream end of the cavity; they output a signal centered at 3GHz with a bandwidth of 5GHz. The electromagnetic field response of the device was then measured for 200ns. The fields were measured along the device, and the two-dimensional FFT was performed to obtain the intensity of the field as a function of frequency and wavenumber. Ge's calculated dispersion curves were compared to the dispersion relationship found in this thesis, yielding insight into how that design may be constructed.

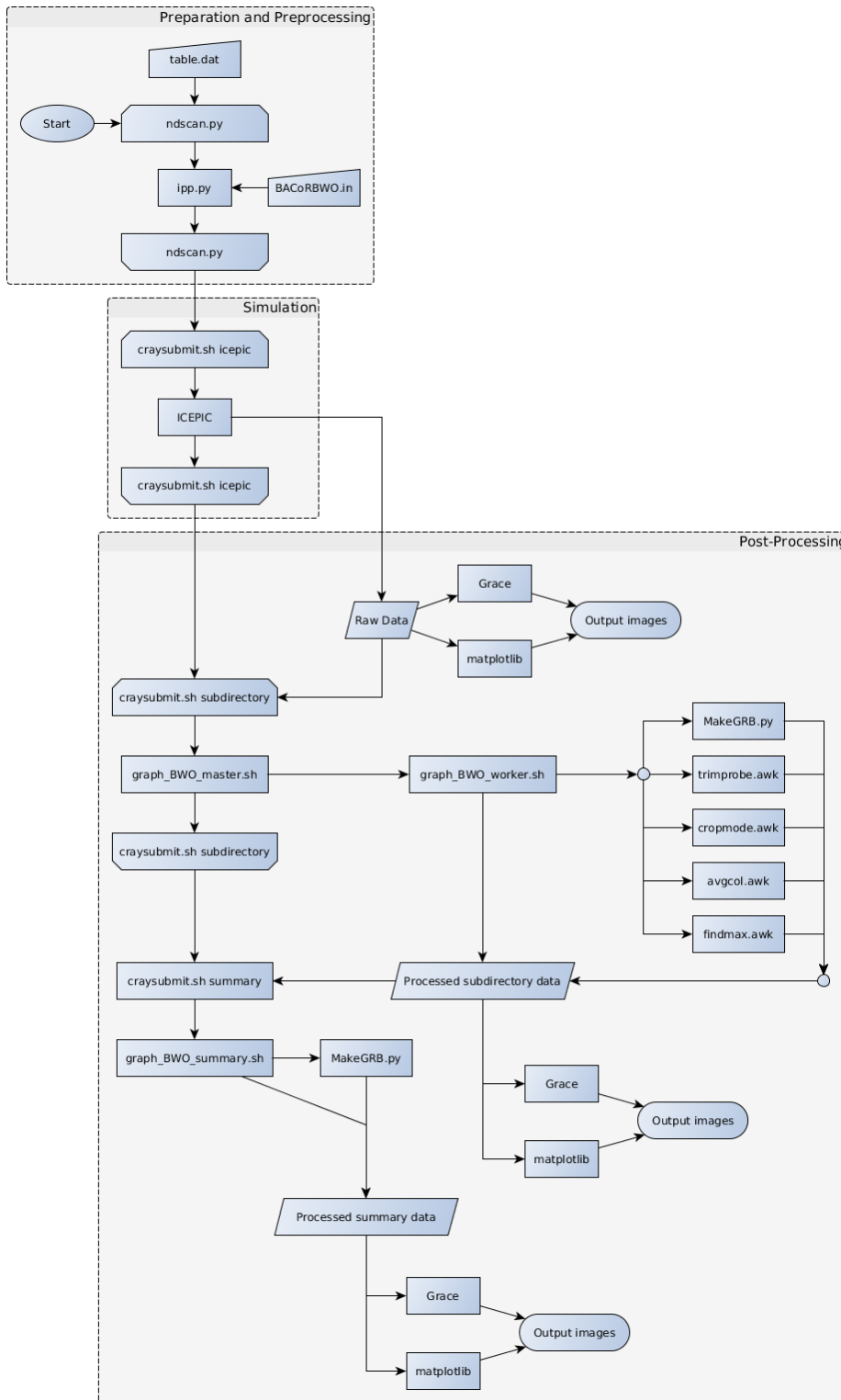


Figure 3: Flowchart detailing the preprocessing, simulation, and post-processing pipeline. Each processing node displays the name of the script used in that step.

Automation of Data Processing and Visualization

An overview of the data processing pipeline is shown in Figure 3 on the previous page. It is broken into three distinct steps, which are: preprocessing, simulation, and post-processing. The preprocessing step includes any work done in advance of running the ICEPIC simulations. Some of these tasks are the programming of the ICEPIC model and the construction of a regime of simulation permutations that will be run. The simulation processing group consists of uploading the simulation files to the supercomputers, enqueueing the simulation jobs to the supercomputer's job list, as well as running ICEPIC itself. The post-processing step is where any data manipulations or calculations take place and where the data is visualized and summarized into formats that are easily interpreted by the user.

Stand-alone PIC codes (such as ICEPIC) generally do not include any sort of data visualization tools as part of their packages; as such, the appropriate post-processing needs to be implemented by the end-user. Post-processing, in this context, should be taken to mean any form of data manipulation (such as an FFT) or visualization (such as graphing the aforementioned FFT and saving the resulting image) that is performed after the simulation is complete. In most cases, ICEPIC records data as one plain text file for every diagnostic requested in the input file; the timecourse is the

first column of the file, and the following columns are the recorded data. These data files can vary quite a bit in size, depending on the type of diagnostic requested, the measurement precision, and the measurement interval. Different types of diagnostics will output different amounts of data; for example, a voltage diagnostic will only have two columns (time and voltage), whereas an E- and B-Field probe will have seven (time, E_x , E_y , E_z , B_x , B_y , and B_z). Field and particle diagnostics are the typical exceptions to the one-file-per-diagnostic rule, simply because the large amount of data would cause the resulting file to become too difficult to work with. Therefore, these diagnostics are saved as separate files for each measurement interval. Because the data output is computer generated, the format is predictably similar; this allows for the visualization post-processing to be done in a repeatable manner, which means that this can then be automated. This becomes important when working with large numbers of simulations that all need the same processing executed. The team at the AFRL had already developed some post-processing and automation tools, and around these a new set of scripts were created in order to automate and streamline the entire process as well as provide additional functionality.

When discussing simulations being run in ICEPIC, there are two different types of input files needed; these are generated in the preprocessing step. The actual data file that ICEPIC uses as its input to initialize the simulation is most often located in its own unique subdirectory and each file usually has the same name, “ice.dat”. These files will be referred to in this paper as the ice.dat files. They are usually not directly created or modified by humans; the process of creating these files is mostly automated by the `ipp.py` (usually called `ipp`) and `ndscan3.py` (usually called `ndscan`) scripts. Both of these scripts were written by Dr. Peter Mardahl at the AFRL, with minor modifications by the author of this paper. `ipp` and `ndscan` use a master simulation input file, referred to as an “ICEPIC input file”, “input file”, or “.in file”, to orchestrate the creation of each unique ice.dat file. This abstraction is required because the input

files are not written in a format that ICEPIC can interpret; ICEPIC cannot evaluate variables, loops, or other structures in the input files. In order to ease the creation process and allow users to quickly change simulation values, `ipp` was written to convert a parametrized input file with logic controls (if-then statements, for loops, etc) and variables into a format readable by ICEPIC by evaluating those variables and logical control structures into the static `ice.dat` file. In order to build and run a useful set of simulations and compare them, a “parameter scan” or “parameter sweep” must be specified. For example, if a researcher wished to examine the behavior of a BWO with respect to the strength of the confining magnetic field, several simulations, each with unique values of magnetic field strength, would need to be run. The way in which this is done is by specifying a table of parameters (usually named “`table.dat`” – no relation to the `ice.dat` files referred to previously) for use by `ndscan` that contains the name of each parameter to change, as well as what values to change those parameters to. Continuing the previous example, to vary the magnetic field strength from 0.8 to 1.0 Teslas in increments of 0.1 Teslas, the `table.dat` would include this line: “`B_Field B 0.8 0.9 1.0`”. The first column, “`B_Field`” is the name of the variable in the input file that is being scanned over, the second column, “`B`”, is an abbreviation of the variable that will be used to give each simulation a unique subdirectory name, and the remainder of the columns are the values to which the specified variable will be set. Multiple variables can be specified, and a unique simulation will be created for every combination of variables possible. `ndscan` would have created three unique simulations in the previous example; if another line were added to the `table.dat`, for example “`Voltage V 700 800`”, then 6 unique simulations would be created, one for each possible combination of the variables “`B_Field`” and “`Voltage`”.

Once the preprocessing is concluded, there will be a top-level simulation directory, and under that directory subdirectories containing the `ice.dat` files for each individual simulation. This group of simulations, or “job” as it is usually referred to, next

needs to be submitted to the job queue on a supercomputer. The Department of Defense's High Performance Computing machines are structured differently from a typical desktop computer. Each supercomputer is composed of a number of computing nodes, each of which contains a number of processing cores. Each node is basically an independent computer, but the difference is the high-speed interconnects between the nodes that allow them to act in concert. As an example, the supercomputer "Conrad" has 1,523 computing nodes, containing 32 processing cores per node, for a total of 48,736 total available processing cores. Jobs are submitted to the queue, and based on the job urgency, time required (anywhere from 1 hour to 168 hours), and processing nodes required (minimum of 1, maximum of 250), the system reserves compute nodes and schedules a time window for the job to execute. The process by which this job scheduling request takes place is somewhat complicated and is very specific to each supercomputer as well as each different research department requesting supercomputer time. Automating this job queueing process was necessary to efficiently use the supercomputers; to this end, the `craysubmit.py` script (referred to as "craysubmit") was formulated. This script's core functionality was adapted from an existing script (again authored by Dr. Mardahl), but was substantially reworked and expanded by this author in support of the work in this paper. In its totality, `craysubmit` submits jobs to any supercomputer desired, taking into account each one's specialized requirements and restrictions, then it creates the necessary job submission file (which includes such things as the number of processors required and hours needed), creates the scripts that actually run the job's programs (such as ICEPIC) once they wait in the queue, copies the files needed (other scripts, ICEPIC files, etc) for the job to the appropriate place on the supercomputer, enqueues the job, then, once that job is complete, does the same for the next job in the pipeline.

There are three different types of jobs that can be submitted to the supercomputers by `craysubmit`. All three require the job submission steps described in the previous

paragraph. When `craysubmit` is passed the argument `icepic`, it submits an ICEPIC simulation job to the supercomputer, the job runs, and the raw ICEPIC data output is stored. When `craysubmit` takes the argument `subdirectory`, a job to process the ICEPIC output data into images (or other usable files) is submitted. This is quite a bit more programmatically complicated than running an ICEPIC simulation; there are several different graphing and file manipulation scripts that must be executed in a specific manner. This type of job is done on the supercomputer (and not locally) for two reasons, the first is that transferring all of the raw ICEPIC data from the supercomputer to a local machine would take an inordinate amount of time, secondly, the supercomputer's speed (even on just one compute node) on these types of file manipulation jobs are orders of magnitude faster than on a normal computer due to the extremely fast storage media employed therein. The last type of `craysubmit` job, the `summary` job, is of a similar function and complexity to a `subdirectory` job; it creates summary graphs and statistics from the `subdirectory` job's output files along with every ICEPIC simulation that was run previously.

When the `craysubmit` script is called in ICEPIC mode, the submitted job runs an ICEPIC simulation for every permutation of the simulation, and, once that is finished, a `craysubmit subdirectory` job is "pipelined" onto the job queue. This means that the `subdirectory` job is automatically submitted to the queue (without any human intervention) by the `craysubmit` script after the ICEPIC commands have all finished running. This is done to save researcher's time and effort; rather than having to manually submit new job types once the previous job finishes, the submission is done automatically in the correct order and format. Once the `craysubmit subdirectory` job has gone through the job queue and has begun running, each individual processing node is controlled by an instance of the script `graph_bwo_master.sh`. This master script, in turn, controls one instance of `graph_bwo_worker.sh` for every processing core in the node; each of which is assigned to process one specific simulation's sub-

directory. The worker script controls all graphing and file manipulation functions for that subdirectory.

File manipulations (such as FFTs or running averages) and data visualizations are carried out by a multitude of different script files. There are four AWK scripts used to perform file manipulations within the scope of the worker script: those are `trimprobe.awk` (removes extraneous data from the EB probe files), `cropmode.awk` (removes extraneous data from TE and TM mode power files), `avgcol.awk` (returns the average of a column in a file) , and `findmax.awk` (returns the max value found in a column and its location in a file). AWK is used here simply because it is well suited to file manipulation with very little overhead. The remainder of file manipulations are carried out by various functions within the `MakeGRB.py` script, which is a collection of 36 python functions, all with differing utility. As an example, the function `MakeGRB.dofft` performs an FFT on a dataset in a file, then saves that FFT in a new text file so that it can later be graphed by other functions. A summary of the file manipulation and data visualization functions in `MakeGRB.py` is shown in Table 1 on page 19.

Two different programs provided basic data visualization capabilities: the first was Grace [23], the second was the Matplotlib library for Python [24]. Grace provides a batch mode program (useful as an interface to automation scripts, in this case BASH was used) as well as a graphical user interface (GUI) that is useful for tweaking the final image if needed. Matplotlib is used exclusively from Python scripts and is most useful in place of Grace when calling external functions in Python would be computationally or programmatically cumbersome, or, when a pure Python implementation is desired (usually for portability).

Grace is a graph plotting tool that can be used to graph an arbitrary number of data sets in two dimensions. Detailing the GUI is outside the scope of this docu-

ment; batch-mode Grace (i.e. the command-line, non-interactive utility, referred to as “gracebat” here and by the documentation) will be focused on, as that was the primary method in which Grace was used. `gracebat` is simply a way for automated scripts to interact with Grace without any user input. It can be used with many configuration options; however, for the most part, these command-line options remained static, each graph’s settings (such as text size, symbol colors, etc) are specified in a separately written command file. This command file executes the same commands as the GUI, but in a programmatic, non-interactive way. For example, if, in the GUI, one was to change the label on the x-axis to “Voltage”, that would be done by right-clicking the mouse on the axis, finding the appropriate setting, and typing in the new label string. Behind the scenes, what Grace does is execute the command `xaxis label Voltage`. Every such GUI action has a corresponding text command and it is here (under-the-hood, so to speak) that the Grace automation can take place; these commands are procedurally generated for each analysis requested. Table 1 contains several examples of python functions that write these Grace command files.

Table 1: Summary of File Manipulation and Data Visualization Functions in the Script `MakeGRB.py`.

Function Name	Brief Description
<code>assigncode</code>	Takes a parameter name and value and returns the relative position of that value among the other values for that parameter in the <code>table.dat</code>
<code>color</code>	Creates a user-defined HSV color gradient and returns it in a format usable by <code>xmgrace</code>
<code>convert_size</code>	Converts a size index to a proper size (float) usable by Grace
<code>dofft</code>	Performs an FFT on a given data set. The resulting data is saved as a new file
<code>fileops</code>	Calculates the efficiency of a particular simulation and saves that data as a new file
<code>Get_Timestep</code>	Opens the ICEPIC log file (<code>ice.log</code>) and pulls out the simulation's time step value
<code>Make_Legends_Subdir</code>	Configures plot legends and calls <code>write_sets</code> and <code>mkGRB</code> in order to configure a plot's parameters. Used for subdirectory post-processing
<code>Make_Legends_Summary</code>	Similar to <code>Make_Legends_Subdir</code> , except only used for summary post-processing jobs
<code>Make_Point_File</code>	Takes a file with one data set and extracts the maximum or average
<code>mkGRB</code>	Parses the title of a graph and creates a Grace configuration file containing the appropriate axis labels and scaling, zoom level, etc
<code>param_extract</code>	Creates a coordinated color code, ensuring that the colors, symbols, and patterns are consistent throughout all ICEPIC simulations
<code>parse_table</code>	<code>parse_table</code> opens the <code>table.dat</code> file, parses it, and returns the data in an array
<code>parse_title</code>	Used with <code>mkGRB</code> . Takes a graph title e.g. "Efficiency vs Time" and outputs the proper scale factors, labels, tick spacing, etc
<code>part_field_plot</code>	Graphs a series of particle images (such as electron position) and field images, then creates a time-series video from those images
<code>plotgrace</code>	Runs Grace to create the desired images
<code>pull_from_icedat</code>	Takes a list of parameters and searches the <code>ice.dat</code> file for them and returns their values
<code>running_mean</code>	Calculates the running average over N points of an array
<code>save_leg</code>	Mainly used to run the <code>mkGRB</code> function and save the output; contains some accessory functionality
<code>sort_legend</code>	Sorts the legend based on passed parameters
<code>write_and_output</code>	Parses the values in the <code>table.dat</code> file and saves each permutation of each parameter in each subdirectory
<code>writedat</code>	Writes a file containing a single data point to be graphed by the function <code>Make_Legends_Summary</code>
<code>write_points_files</code>	Writes a file containing two points (such as efficiency and voltage) to be graphed by the function <code>Make_Legends_Summary</code>
<code>write_sets</code>	Outputs the set characteristics for Grace like symbol, color, pattern, etc

Results

Simulation of the BACoRBWO started with re-creating the original simulation done by Ge et al referenced in the introduction. Initial two-dimensional simulation results were inadequate to properly represent the device¹; therefore all simulations shown were performed in 3D.

To explore the geometry dependent behavior of the BWO, a set of simulations was created for varying lengths of the inner conductor. The voltage and current were held to their original values ($760kV$ and $9.6kA$), and the inner conductor length was scanned from $10mm$ up to $490mm$ by increments of $10mm$. The power and dominant frequency were measured; the results of this scan are shown in Figure 6 on page 23.

Shown in Figures 4 and 5 on page 23 are the results found for output power for six different configurations of the BACoRBWO. The solid blue lines on each graph show the power output using the value for inner conductor length specified in Ge's 2014 work. The red dashed line shows the maximum power output found by scanning the simulations over possible values of inner conductor length (see Figure 6 on page 23 for this scan data). The black triangles mark the original peak power values found by Ge. Note that the outputs using the original specifications show significantly less power than that found by Ge and that the dominant frequencies are completely different as

¹2D simulations did not oscillate at more than 500MW for any frequency or value of inner conductor length. 3D simulations, however, performed closer to expected values based on the cited values in Ge's work.

well. Finding the optimum length of inner conductor improves power output but does not change the output frequencies to those expected. Figures 10 and 11 on page 24 show total power output of the device as a function of time in both the coaxial and hollow operation mode.

Figures 8 and 9 on page 24 show the efficiency of the power output of the BWO as well as the frequency of that power output as the beam voltage is varied. The voltages vary from $310kV$ up to $760kV$ in increments of $50kV$, with the blue dots representing the lowest voltage, and transitioning up the spectrum to the red dots representing the highest voltages on the graph. The highest voltages operate the most efficiently, and the operating frequency of any configuration oscillating in a meaningful way (greater than 5% efficiency) oscillates at a consistent frequency regardless of voltage. Despite frequency being on the x -axis (traditionally reserved for the independent variable), both frequency and efficiency are plotted as a function of changing voltage. The highest efficiencies of 15% for the coaxial BWO and 26% for the coaxial BWO are produced at the highest voltage tested ($760kV$ – the value used by Ge’s 2014 work). The operational frequencies are very stable, only changing bands once the diode voltage drops below $610kV$.

A graph of the beam’s time-averaged kinetic energy per-particle as a function of distance along the BWO structure is shown in Figure 12 on page 27. The kinetic energy of an electron at emission from the electron gun is approximately $1.2 * 10^{-13} J$ and the average final kinetic energy at impact with the extractor is $0.7 * 10^{-13} J$, meaning that, at most, 40% of that kinetic energy can be converted into field energy, assuming no other losses in the BWO.

Two graphs for instantaneous beam velocity were calculated, one for $V = 760kV$

(Figure 7 on the next page) and one for $V = 660kV$ (Figure 13 on page 27). The speed of the particles in the high-voltage graph, for most axial locations, is close to $2.8 - 2.9 * 10^8 m/s$, or approximately $0.95c$. In the low voltage graph, electron speed was about $2.6 * 10^8 m/s$ or $0.87c$.

Figures 14 and 15 on page 28 show the calculated dispersion curves for the coaxial and hollow (respectively) BACoRBWO configurations. The dashed line showing $v_p = 0.95c$ was derived from the velocity graph, Figure 7 on the following page. The solid line on the graph shows the dispersion curve estimated from Ge's work and published dispersion curves.

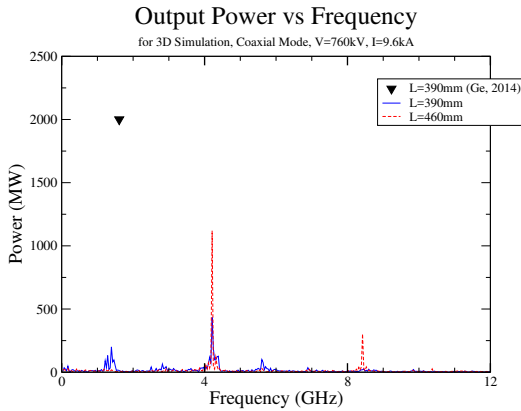


Figure 4: Power Spectrum of the Coaxial-Mode BACoRBWO.

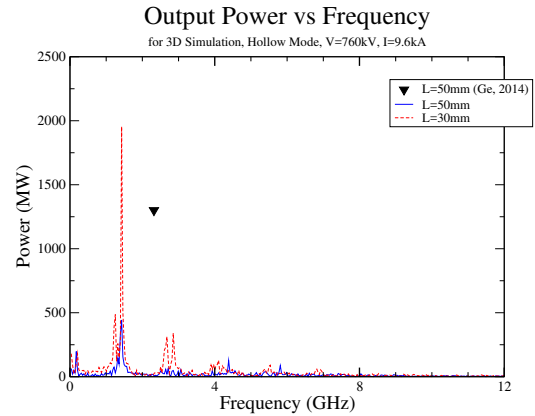


Figure 5: Power Spectrum of the Hollow-Mode BACoRBWO.

Power and Frequency vs Inner Conductor Length

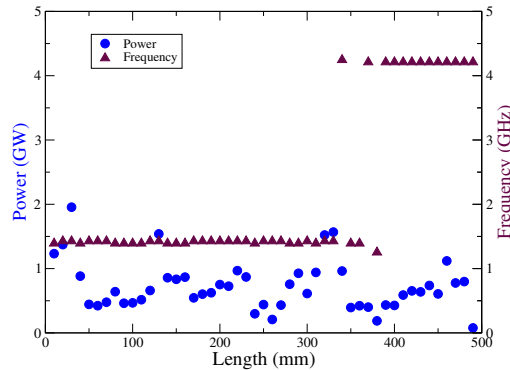


Figure 6: Power and frequency as a function of inner conductor length. The blue circles show the power and the red triangles show the frequency as the inner conductor length is varied from 10mm up to 490mm in increments of 10mm . The band transition length for inner conductor is a range of values between 330mm and 390mm ; in this range, the output power drops and the frequency becomes unstable as different modes compete in the device.

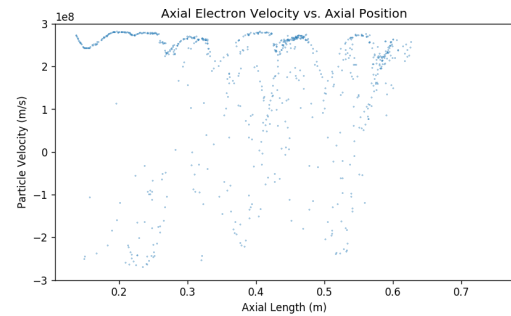


Figure 7: Instantaneous electron velocity as a function of distance along the BWO for a beam voltage of 760kV . Average electron velocity here is roughly $2.8 \times 10^8\text{m/s}$ or $0.93c$. Several distinct areas of deceleration (energy transfer from electron kinetic energy to fields) can be seen. This graph also shows that the electron velocity is, for a minority of the electrons completely turned backwards; the apparent reason for this is an accumulation of space charge at the deceleration points that is strong enough to throw some electrons back towards the electron gun.

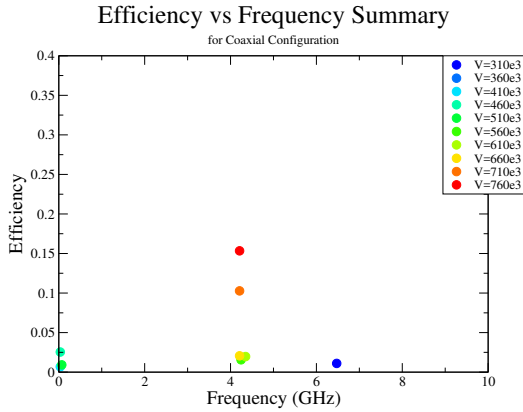


Figure 8: Efficiency and Voltage vs. Frequency (Coaxial Configuration).

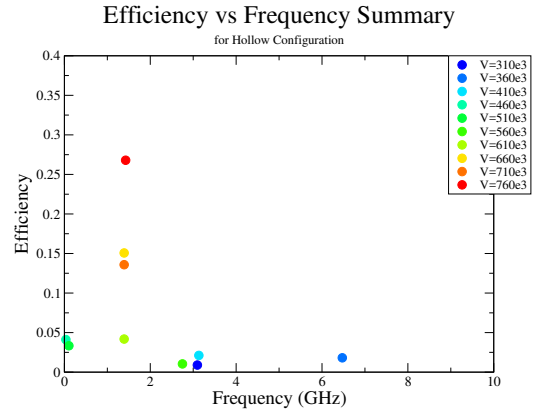


Figure 9: Efficiency and Voltage vs. Frequency (Hollow Configuration).

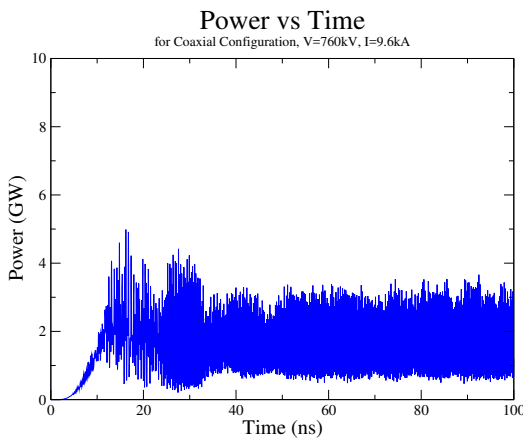


Figure 10: Power Output vs. Time (Coaxial). Note here the fact that the power does not at any point reach 0. This means that a non-transverse mode is propagating out the waveguide.

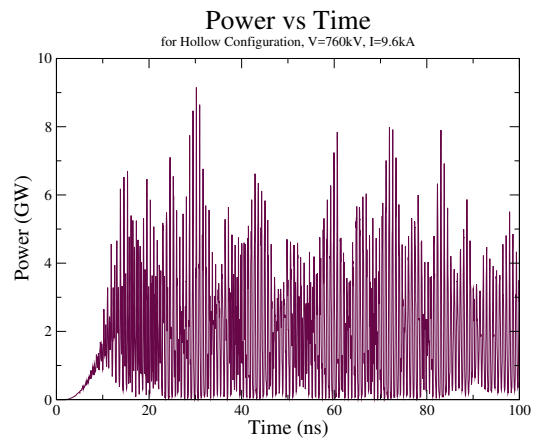


Figure 11: Power Output of the BWO as a function of time (hollow configuration). The output is noisy, note the low-frequency, high-power spikes.

Discussion

Using the exact parameters specified by Ge's paper, simulation results were disappointing. Figure 4 on page 23 shows that the coaxial configuration of the BWO oscillated most powerfully at $4.1GHz$, with an output power of about $500MW$ at that frequency, giving an efficiency of 7%. Of particular note is the unsuppressed signal at $1.4GHz$ emitting from the BWO. This indicates that interference between output modes exists and needs to be addressed. Figure 5 on page 23 shows the hollow configuration's power output spectrum; it again operates at $500MW$ and 7% efficiency, but at $1.4GHz$. The fundamental output frequency here is within 15% of the value found by Ge ($1.61GHz$) *for the coaxial mode*; this indicates that our simulation is not exciting the exact same modes as the reference device, but that at least one of the same modes exist. Clearly, there is a missing piece of the puzzle.

The graph of power and frequency versus inner conductor length shown in Figure 6 on page 23 shows a fairly stable operating frequency of approximately $1.4GHz$ from $10mm \leq L \leq 320mm$, where L is the inner conductor length. When $330mm \leq L \leq 390mm$, the BWO enters a band transition zone where output power drops and frequency output becomes unpredictable due to mode competition. From $400mm \leq L \leq 490mm$ the device enters another region of frequency stability, operating at $4.2GHz$. The power output stability is very erratic with respect to changes in the inner conductor's length; power varies from $100MW$ up to $2GW$ as the length of the

conductor is altered. Irregular output power was seen by Ge; in his paper, the power output ranged from $1.5GW$ to $2.5GW$ which is quite a large range, but not quite as large as the power output variability seen here. Ge's published paper uses $L = 50mm$ and $L = 390mm$ as optimum conductor lengths to excite the two different frequencies, but note that in these simulations, those two particular values of inner conductor length provide quite poor output power. Better choices in this particular case might be $30mm$ (to operate at $1.4GHz$ and $1.9GW$ - 26% efficiency) and $460mm$ (to operate at $4.2GHz$ and $1.1GW$ - 15% efficiency). This does not answer the question of why the $2.3GHz$ output seen by Ge does not manifest, but the device as it stands would still be considered band-agile, and is therefore still useful.

The graphs of efficiency and operational frequency as a function of voltage (Figures 8 and 9 on page 24) show that the device output is very stable with respect to the input voltage. The device operates at the same frequency from voltages from $760kV$ down to $610kV$ (albeit at reducing efficiencies), thus giving credence to Kitsanov's assertion that voltage tuning is largely ineffective in relativistic BWOs [9] and to the idea of a mechanically-tunable BWO in general.

A spatial analysis of the beam energy content shows that, as the electrons in the beam pass through each successive segment of the SWS, they give up kinetic energy and emit at least some part of that energy as RF power. The graph, Figure 12 on the next page, shows the time-averaged energy of each particle in the beam as a function of axial distance. The electrons lose about 40% of their energy on their path through the BWO, and the highest efficiency seen in these simulations was 26% (for the coaxial configuration). The conclusion, then, is that the electrons lose 14% of that energy to wasteful ends, of which there are several. The electron velocity graphs of Figure 7 on page 23 and Figure 13 on the next page show electrons with highly negative velocities – these electrons have left the confinement of the beam

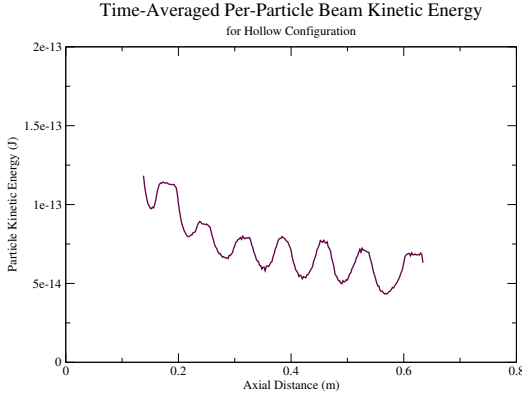


Figure 12: The time-averaged kinetic energy of each particle in the electron beam as a function of axial distance. The left-most point is where the beam is emitted from the electron gun. From this maximum, as the electrons travel along the SWS, they give up their kinetic energy to the E- and B-fields. A decrease in kinetic energy of about 40% is seen here.

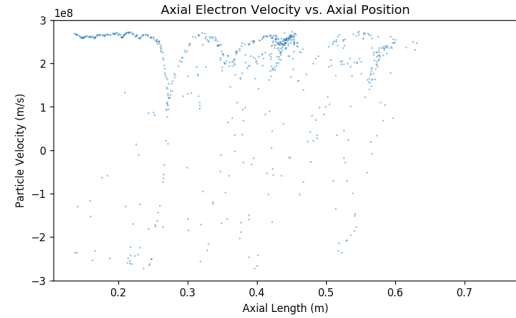


Figure 13: The instantaneous axial electron velocity as a function of axial distance when beam voltage is $660kV$. Although the maximum electron velocity remains fairly constant throughout the SWS, the range of electron velocities increases drastically (lowering the average kinetic energy, which is behavior also seen in Figure 12 as well as Figure 7 on page 23). Average beam velocity is approximately roughly $2.6 * 10^8 m/s$ or $0.87c$. This graph (consistently with Figure 7 on page 23) shows electrons that leave the beam and get turned back upstream towards the electron gun, which are not counted in Figure 12.

and are travelling back upstream towards the electron gun. This is likely due to a large enough space charge accumulating to completely repel those electrons. The energy used to accelerate those electrons back upstream would be one source of wasted energy. Another is the wasted power output in spurious frequencies. Examining Figures 4 and 5 on page 23 shows non-trivial noise frequencies present in the output signal. Using as an example Figure 5, there is 2000MW of power in the dominant frequency, and about 1000MW of power in other frequencies. This means that, since that particular simulation was found to be 26% efficient, that 50% of that 26% (that is to say, 13%, which was not included in the 26% efficiency calculation) was waste energy. The sum of the percentages of useful RF (26%) and waste RF (13%), adds up to 39%, which accounts for nearly all of the 40% of the kinetic energy that the electrons

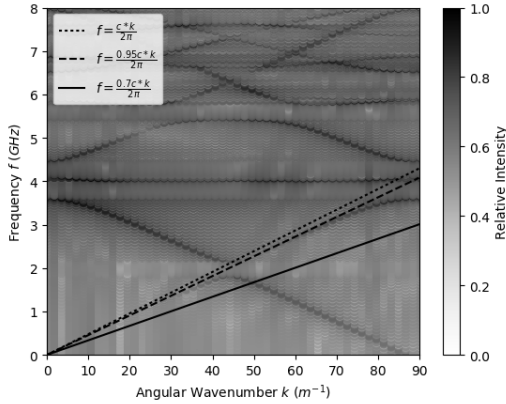


Figure 14: Dispersion Diagram (Coaxial Configuration).

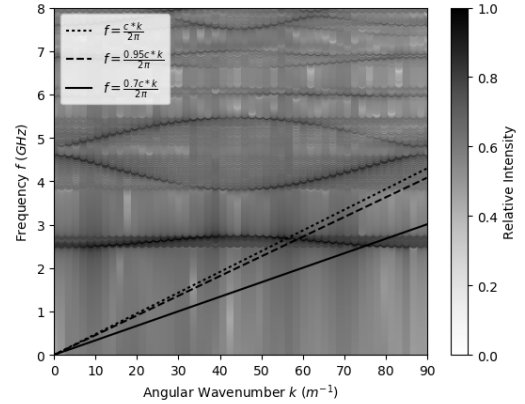


Figure 15: Dispersion Diagram (Hollow Configuration).

lost while travelling through the BWO. There are very clearly some improvements to be made here regarding the wasted RF emission, which seems to be the main source of inefficiency. The other path to consider when improving the overall efficiency would be to extract more kinetic energy from the electrons overall, so that even if a large portion of the energy is still in wasted RF output, there is more total energy to work with.

The dispersion diagrams for the BWO are shown in Figures 14 and 15. The dotted line on each graph shows the light line (i.e. where the phase velocity, $v_p = c$), the dashed line shows the beam line found in these simulations ($v_p = 0.95c$), the solid line shows the beam line estimated from Ge’s 2009 work on the BACoRBWO and its dispersion characteristics [20] ($v_p = 0.7c$). The fainter lines illustrate the modes of the BACoRBWO as simulated in this paper and found by a dispersion analysis (detailed in the Methods section of this paper). Interesting to note for the coaxial plot is the fact that the beam line calculated for this device from the ICEPIC simulations ($v_p = 0.95c$), completely misses the lowest mode on the graph, the “quasi-TEM” mode referred to by both Ge and Xiao [20, 15, 12]. This is consistent with other results obtained in this analysis, as the higher velocity beam line first intersects with a strong

interaction point at just over $4GHz$. The first mode that the beam could possibly interact with is called the “A” mode [20, 15, 12], but the region of the curve where the interaction would take place is particularly weak so the beam passes through this mode as well without exciting the structure, and oscillation takes place in a different mode even further up the beam line. However, the group velocity at this interaction point is positive, which means that the RF wave that forms is not a backward wave, but rather a forward wave. This is not inherently problematic; other tubes, such as the TWT, operate in the forward wave region, but it does belie the name of Backward Wave Oscillator. The lower-velocity beam line (i.e. the line estimated from Ge’s publications) interacts in the quasi-TEM mode at approximately $1.5GHz$, this seems to be within a reasonable deviance of Ge’s frequency of $1.6GHz$ for this configuration. The hollow dispersion curves and the low velocity beam line also match up quite well with Ge’s oscillation at $2.3GHz$ for hollow operation - however, the measurements from the hollow BWO simulated here are anomalous. It was found to oscillate at $1.4GHz$, but there is not present on the dispersion diagram any such mode that could cause that frequency to become excited. Considering these conclusions with those discussed previously regarding voltage tunability of the RBWO, lowering the beam voltage does not lower the beam velocity enough to make a meaningful difference in what modes the beam line intersects.

The graphs of power as a function of time for each of the two BWO configurations are shown in Figures 10 and 11 on page 24. Keeping in mind that the output power is proportional to the E-field (\vec{E}) cross the B-field (\vec{B}), useful information in the graphs becomes obvious. When the magnitude of either \vec{E} or \vec{B} in a transverse direction (X or Y here) instantaneously crosses 0, the power output in the direction of propagation (Z here) will then go to 0; the power output of the hollow device shows this behavior, leading to the conclusion that a transverse mode of some sort is dominant (which is generally desirable for devices of this type) for the most part, but there is a low

frequency flutter pushing the power output off of the x-axis slightly. This is indicative of a poorly suppressed hybrid mode interfering slightly with the transverse mode's output, but not enough to completely dominate it. Conversely, the coaxial device's power never drops to 0 as it oscillates (i.e. there is a dc offset to the waveform), meaning that it is operating in a hybrid mode in which there is a Z -component to both \vec{E} and \vec{B} . This is not necessarily problematic, as a useable RF signal can still be obtained, but with reduced efficiency as compared to the transverse wave output in the hollow device.

Conclusions

The Band-Agile Coaxial Relativistic Backward-Wave Oscillator described and simulated in this paper operates with a high degree of frequency stability within two different bands. There is a large amount of wasted power generated by this device – about 60% of the electron kinetic energy is left totally unutilized, and about 1/3 of the electron kinetic energy that gets converted into RF is wasted in production of noise frequencies in the output, for a maximum efficiency of 26% with ideal parameters.

There are many reasons for why the design published by Ge [16] and the device described in this paper behave very differently, the first of which is the fact that these simulations were run in different software packages. ICEPIC and KARAT have both been validated by real-world testing of devices designed in the softwares, however, ICEPIC (and one can only assume KARAT, as well) has a near-labyrinthine collection of configuration options, many of which will very noticeably affect the simulation results. Without a side-by-side comparison of the two softwares running the same simulation, the results will be difficult to compare. Another explanation for the discrepancy is simple oversight on behalf of the submitting institution. Similar devices have been actively researched and published by the NUDT since 2009 (see [14, 19, 20, 21, 15]), it is conceivable that an out-of-date figure was included in the 2014 publication, either unintentionally or with the intent of purposeful obfuscation of the device parameters since such a device might be seen as important to national

security by the NUDT.

Future work should, first, determine the reason for the discrepancies between this BACoRBWO and its antecedent device at the NUDT. Exploration of geometrical modifications could be in order, increasing the periods of the SWS, changing the beam drift distance, and of course the overall dimensions of the device are viable options. Once that determination is made, then improvements to the efficiency and operation of the device can be made – perhaps even the prototyping of a tri-band BACoRBWO (L, S, and C band) combining the findings here with those made rectifying the frequency anomalies.

All that being said, the designed backward-wave oscillator is operable in the L-band at 1.4GHz and 1.9GW and also in the C-band at 4.1GHz and 1.1GW. Although the device's power output spectrum was unexpected based on existing literature and BWO designs, this particular design will satisfy the AFRL's requirement for a high-power multi-band HPM source.

Bibliography

- [1] P. Palluel and A. Goldberger, "The o-type carcinotron tube," *Proceedings of the IRE*, vol. 44, no. 3, pp. 333–345, 1956.
- [2] S. Bugaev, V. A. Cherepenin, V. Kanavets, A. Klimov, A. Kopenkin, V. Koshelev, V. Popov, and A. Slepko, "Relativistic multiwave cherenkov generators," *IEEE transactions on plasma science*, vol. 18, no. 3, pp. 525–536, 1990.
- [3] J. A. Nation, "On the coupling of an high-current relativistic electron beam to a slow wave structure," *Applied Physics Letters*, vol. 17, no. 11, pp. 491–494, 1970.
- [4] Y. Carmel, J. Ivers, R. Kribel, and J. Nation, "Intense coherent cherenkov radiation due to the interaction of a relativistic electron beam with a slow-wave structure," *Physical Review Letters*, vol. 33, no. 21, p. 1278, 1974.
- [5] N. Kovalev, M. Petelin, M. Raizer, A. Smorgonskii, and L. E. Tsopp, "Generation of powerful electromagnetic radiation pulses by a beam of relativistic electrons," tech. rep., Lebedev Inst. of Physics, Moscow, 1973.
- [6] V. Ivanov, S. Kremontsov, V. Kutsenko, M. Raizer, A. Rukhadze, and A. Fedotov, "Investigation of a relativistic cerenkov self-generator," *Zh. Tekh. Fiz.*, vol. 51, pp. 970–975, 1981.
- [7] A. V. Gunin, A. I. Klimov, S. D. Korovin, I. K. Kurkan, I. V. Pegel, S. D. Polevin, A. M. Roitman, V. V. Rostov, A. S. Stepchenko, and E. M. Totmeninov, "Relativistic x-band bwo with 3-gw output power," *IEEE transactions on plasma science*, vol. 26, no. 3, pp. 326–331, 1998.
- [8] A. Gaponenko, K. Karlik, S. Kitsanov, A. I. Klimov, I. Konovalov, S. Korovin, G. Mesyats, I. V. Pegel, S. Polevin, D. Proskurovsky, *et al.*, "Lengthening of microwave pulse in a 3-gw relativistic bwo," in *2000 13th International Conference on High-Power Particle Beams*, pp. 730–733, 2000.

- [9] S. A. Kitsanov, A. I. Klimov, S. D. Korovin, V. V. Rostov, and E. M. Tot'meninov, "Relativistic bwo with enhanced frequency tunability," *IEEE transactions on plasma science*, vol. 33, no. 5, pp. 1685–1689, 2005.
- [10] L. Moreland, E. Schamiloglu, R. Lemke, A. Roitman, S. Korovin, and V. Rostov, "Enhanced frequency agility of high-power relativistic backward wave oscillators," *IEEE transactions on plasma science*, vol. 24, no. 3, pp. 852–858, 1996.
- [11] G. Sotnikov and T. Y. Yatsenko, "Space charge limiting current of an electron beam transported in a coaxial drift chamber," *Technical Physics*, vol. 47, no. 5, pp. 535–538, 2002.
- [12] R. Xiao, Y. Lin, Z. Song, C. Chen, and G. Liu, "Theoretical study of a plasma-filled relativistic cerenkov generator with coaxial slow-wave structure," *IEEE Transactions on Plasma Science*, vol. 35, no. 5, pp. 1456–1466, 2007.
- [13] R. Xiao, G. Liu, Y. Lin, and C. Chen, "Analytic theory of relativistic high power microwave generator with coaxial slow wave structure.," *Qiangjiguang Yu Lizishu(High Power Laser and Particle Beams)*, vol. 18, no. 2, pp. 241–244, 2006.
- [14] X. Ge, H. Zhong, B. Qian, J. Zhang, Y. Fan, T. Shu, and J. Liu, "Dispersive characteristics and longitudinal resonance properties in a relativistic backward wave oscillator with the coaxial arbitrary-profile slow-wave structure," *Physics of Plasmas (1994-present)*, vol. 16, no. 11, p. 113104, 2009.
- [15] X. Ge, H. Zhong, B. Qian, J. Zhang, L. Gao, Z. Jin, Y. Fan, and J. Yang, "An l-band coaxial relativistic backward wave oscillator with mechanical frequency tunability," *Applied Physics Letters*, vol. 97, no. 10, p. 101503, 2010.
- [16] X. Ge, J. Zhang, H. Zhong, B. Qian, and H. Wang, "The mechanism and realization of a band-agile coaxial relativistic backward-wave oscillator," *Applied Physics Letters*, vol. 105, no. 18, 2014.
- [17] J. D. Blahovec, L. A. Bowers, J. W. Luginsland, G. E. Sasser, and J. J. Watrous, "3-d icepic simulations of the relativistic klystron oscillator," *IEEE transactions on plasma science*, vol. 28, no. 3, pp. 821–829, 2000.
- [18] P. D. Gensheimer, C. K. Walker, R. W. Ziolkowski, and C. D. d'Aubigny, "Full-scale three-dimensional electromagnetic simulations of a terahertz folded-waveguide traveling-wave tube using icepic," *IEEE Transactions on Terahertz Science and Technology*, vol. 2, no. 2, pp. 222–230, 2012.
- [19] X. Ge, B. Qian, and H. Zhong, "Particle simulation of relativistic backward wave oscillator with coaxial extractor [j]," *High Power Laser and Particle Beams*, vol. 4, p. 010, 2009.
- [20] X. Ge, H. Zhong, B. Qian, L. Liu, Y. Liu, L. Li, T. Shu, and J. Zhang, "Transversal and longitudinal mode selections in double-corrugation coaxial slow-wave devices," *Physics of Plasmas (1994-present)*, vol. 16, no. 6, p. 063107, 2009.

- [21] X. Ge, H. Zhong, B. Qian, J. Zhang, L. Liu, L. Gao, C. Yuan, and J. He, “Asymmetric-mode competition in a relativistic backward wave oscillator with a coaxial slow-wave structure,” *Applied Physics Letters*, vol. 97, no. 24, p. 241501, 2010.
- [22] X. Ge, H. Zhong, J. Zhang, and B. Qian, “A high efficient relativistic backward wave oscillator with coaxial nonuniform slow-wave structure and depth-tunable extractor,” *Physics of Plasmas (1994-present)*, vol. 20, no. 2, p. 023105, 2013.
- [23] “Grace home. <http://plasma-gate.weizmann.ac.il/grace/>.” Online; accessed 13-April-2017.
- [24] J. D. Hunter, “Matplotlib: A 2d graphics environment,” *Computing In Science & Engineering*, vol. 9, no. 3, pp. 90–95, 2007.